Study of exciton polariton modes in nanocrystalline thin-films of ZnO using reflectance spectroscopy

J Fryar, E McGlynn, M O Henry, J-P Mosnier

School of Physical Sciences/NCPST, Dublin City University, Glasnevin, Dublin 9, Ireland

We report detailed reflectance studies of the exciton-polariton structure of thin-film nanocrystalline ZnO at low temperatures and compare these data to bulk crystal behaviour. The reflectance spectra are fit using a two-band dielectric response function with a number of different models involving reflected waves in the thin-film and/or excitonic dead-layers. We present matrix forms for the solution of these models, enabling computation of the reflected intensity and other field components. The reflectance of nanocrystalline ZnO differs substantially from that of bulk material, with Fabry-Perot oscillations at energies below the transverse *A* exciton and above the longitudinal *B* exciton. Between these energies we see no evidence of anomalous waves because the strong interaction of the damped exciton with the photon leads to polaritons with substantial damping such that the Fabry-Perot oscillations are eliminated. Good agreement is found between the model and data and the importance of the polariton viewpoint in understanding the reflectance data of nanocrystalline material is clearly seen. The fits provide parameter values that can be compared to bulk crystal parameters, providing a method for quantitative analysis of the films and their potential for applications such as thin-film random lasing or polariton lasing in microcavities.

Short title: Exciton polariton modes in nanocrystalline ZnO

Keywords: exciton, polariton, thin-film, ZnO.

PACS codes: 71.35.-y, 71.36.+c, 78.20.-e, 78.40.Fy

_____Author to whom correspondence should be addressed:

Dr. Enda McGlynn, School of Physical Sciences/NCPST, Dublin City University, Glasnevin, Dublin 9, Ireland. Tel: ++353-1-7005387; Fax: ++353-1-7005384; Email: enda.mcglynn@dcu.ie

1. Introduction

Reflectance spectroscopy is a useful technique in the study of photonic materials since it allows one to deduce exciton energies, resonant damping/broadening parameters, and to understand the effects of strain and other perturbations [1-3]. Hence, examining and modelling excitonic reflectance resonance features is particularly valuable in the study of nanocrystalline thin-films where such effects are of major importance and may strongly affect the potential of the films for optoelectronic device applications [4,5]. There is a substantial amount of prior work on the reflectance properties of II-VI bulk crystals (including ZnO) and thin-films of materials such as CdS and CdSe, where Fabry-Perot oscillations in the film have been examined for the case of a single excitonic resonance with various boundary conditions [6-8]. Given the recent interest in ZnO thin-film growth for optoelectronic device applications [9], we present the necessary equations for a two resonance case (including the effects of coupled *A* and *B* excitonic oscillators) with appropriate boundary conditions in order to model the reflectance spectra of such thin-films for the simplest case of normal incidence. To the best of our knowledge this is the first time that such models have been detailed in the literature for a two-band exciton resonance in thin-film structures. We apply the models presented to both thin-film nanocrystalline material grown by pulsed laser deposition (PLD) on *c*-sapphire and to bulk samples, and discuss the importance of the exciton-polariton viewpoint in interpreting the data. Preliminary reflectance data on these samples has been published previously and the current work expands on the earlier report by detailing the computational models used and applying models including dead-layers for the thin-film structure [10].

We have examined 4 different models in our analysis. Model 1 involves matching the incident and reflected rays with the propagating polariton modes at the crystal interface using electromagnetic boundary conditions in addition to the required "additional boundary conditions" (ABCs). The form of ABC we have used is the so-called "Pekar ABC" with the total polarization due to each exciton branch vanishing at the crystal interface [11, 12], due to confinement of the excitons within the crystal. Model 1 neglects the thin-film nature of the sample and treats the layer as semi-infinite. Model 2 includes reflections from the back surface of the sample and consequent interference effects, again utilising the Pekar form of the ABC at both interfaces.

For Models 1 and 2 we have applied the ABC at the physical layer boundaries. In fact, one would actually expect the classical reflection point of the excitons to lie somewhat deeper in the material as a result of repulsive forces due to image-charge effects. To account for this behaviour we have used the infinite-barrier approximation of *Hopfield* and *Thomas* [11] in Models 3 and 4 which accounts for this deeper-lying reflection point by considering that there exists an infinite potential barrier at a finite distance from the crystal interface through which the excitons cannot penetrate, creating an exciton dead-layer between the infinite barrier and crystal surface. Model 3 takes into account both the thin-film nature of the sample, including exciton dead-layers at front and back surfaces, while Model 4 assumes again a semi-infinite crystal and utilises a dead-layer at the front sample surface (appropriate for bulk samples). Although we have chosen to use Pekar's form of the ABCs, the simultaneous equations shown below can be easily modified for other conditions. The numerical solution of these models gives the reflection coefficient as a function of photon energy and allows calculation of the electric fields due to different photon and polariton modes in various regions of the structure. We find that Fabry-Perot effects must be considered to accurately model experimental data for thin-film samples. Due to the high exciton damping in the case of the thin-film samples reported here, inclusion of dead-layer effects at the film interfaces is not required. In contrast we see that it is necessary to include such dead-layer effects in the case of a bulk ZnO wafer. The fits yield parameter values in good agreement with literature values in the case of the bulk wafer and with independently-measured parameters such as film thickness in the case of the thin-films, where such measurements were possible.

2. Experimental Details

The thin-film samples studied here were grown using the PLD technique. A ceramic polycrystalline ZnO target (99.99%) was ablated using a KrF excimer laser (λ = 248 nm) with a laser energy density of 1.7 J/cm^2, a pulse repetition rate of 10 Hz, and a pulse duration of 26 ns. The target to substrate distance was ~ 4 cm. The ZnO films were deposited on (0001) sapphire substrates at an oxygen (99.99%) pressure of 0.3 mbar (225 mTorr) and the substrate temperature was maintained at 400°C during growth. The film thickness was estimated to be in the 150-200 nm range for all films, based on the calibrated growth rate per laser shot of the PLD system. The samples grown are nanocrystalline with a columnar grain structure with *c*-axis orientation and show evidence of strong electric field damping of the free-exciton (FE) [13]. Some samples were further annealed in O_2 (0.3 mbar) at temperatures of 400°C and 500°C respectively in the growth chamber

immediately after deposition, leading to a consistent increase in grain size (30 → 80 nm) and reduction in FE damping with annealing temperature [13, 14]. The single-crystal material was purchased from the Eagle-Picher Corporation, and was grown using the Seeded Vapor Phase Transport (SVPT) method. More details of the reflectance measurements are given in [10, 13]. No observable change is seen with different polarisations of the incident radiation.

The experimental reflectance spectra were obtained at a temperature of 17 K, with samples cooled using a Janis CCS-500 closed-cycle cryostat and illuminated by an Ealing 150W Xe lamp. The angle of incidence with our experimental arrangement was < 7˚ to the *c*-axis. Reflected light was spectrally analyzed with a Bomem DA8 FT spectrometer fitted with a Hamamatsu R1913 PM-tube. The resolution of the presented spectra is ~ 0.1 meV.

3. Summary of Reflectance Modelling

To model the experimental reflectance data we have used the classical theory of the exciton-polariton interaction given by *Hopfield* and *Thomas* [11]. The three valence bands of ZnO are most commonly assigned to Γ_7, Γ_9, and Γ_7 symmetries in order of energy, respectively, with a single conduction band level giving rise to three exciton bands labelled *A*, *B* and *C* in order of increasing energy [15, 16]. Selection rules indicate that the lowest exciton band will not contribute to the reflectance at normal incidence [16]. Therefore, our spectra at normal incidence may be modelled using a coupled two exciton band model, interacting with the photon mode of the crystal. Applying Maxwell's equations to solve for the transverse modes (since the measurements are taken at normal incidence) one obtains the two-band dielectric response function [11,17]:

$$\frac{k^2c^2}{\omega^2} = \varepsilon_\infty + \frac{\alpha_{A0}}{\varepsilon_0}\left(\frac{{\omega_{AT}}^2}{{\omega_{AT}}^2 + \beta_A k^2 - \omega^2 - i\omega\Gamma_A}\right) + \frac{\alpha_{B0}}{\varepsilon_0}\left(\frac{{\omega_{BT}}^2}{{\omega_{BT}}^2 + \beta_B k^2 - \omega^2 - i\omega\Gamma_B}\right) \quad (1)$$

Here, ω is the angular frequency, *k* is the wavevector, ε_∞ is the static background dielectric constant and ω is the frequency of the incident radiation, α_{A0} and α_{B0} are the static exciton polarizabilities, ω_{AT} and ω_{BT} are the transverse exciton frequencies, and Γ_A and Γ_B are the wavevector-independent damping parameters of the *A* and *B* excitons, respectively. Due to the normal incidence geometry parallel to the *c*-axis, the *k*

values may be considered scalar quantities. The β parameters may be expressed in terms of the exciton effective masses as follows [17]:

$$\beta_{A,B} = \frac{\hbar \omega_{AT,BT}}{m_{A,B}^{*}} \tag{2}$$

where m^* is the effective mass. In practice one seeks to solve equation (1) for the values of k corresponding to a particular ω. Multiplying across by the two denominators on the right hand side of (1), one obtains an equation cubic in k^2. One may then solve for the three different values of k^2 as a function of ω to give the exciton-polariton dispersion curve (the *k* values are then given by $\pm\sqrt{k^2}$, corresponding to opposite propagation directions). The dispersion curve predicted by eqn. (1) contains upper *B* and lower *A* transverse exciton-polariton branches, and a mixed lower *B*/upper *A* branch due to the coupling of harmonic oscillators as shown in figure 1. The presence of a number of modes at each frequency is the signature of spatial dispersion [11]. The refractive index corresponding to each mode is given by $n_i = \sqrt{\frac{k_i^2 c^2}{\varpi^2}}$, with the sign chosen positive if n_i is purely real, or, more commonly, in the presence of damping and spatial dispersion, chosen to ensure that the imaginary part leads to decay of the field amplitude away from the boundary as in equation (6) below.

There are two frequencies ω for which the value of dielectric constant (i.e. the expression on the RHS of eqn. (1)) becomes zero, corresponding to the longitudinal frequencies of both *A* and *B* excitons, ω_{AL} and ω_{BL} respectively. It is possible to express eqn. (1) in terms of these longitudinal frequencies instead of the static polarizabilities, and in that case one obtains the relations [17]:

$$\alpha_{A0} = \varepsilon_\infty \left(\frac{\varepsilon_0}{{\omega_{AT}}^2} \right) \left({\omega_{BL}}^2 - {\omega_{AT}}^2 \right) \left(\frac{{\omega_{AL}}^2 - {\omega_{AT}}^2}{{\omega_{BT}}^2 - {\omega_{AT}}^2} \right) \tag{3}$$

and:

$$\alpha_{B0} = \varepsilon_\infty \left(\frac{\varepsilon_0}{{\omega_{BT}}^2} \right) \left({\omega_{AL}}^2 - {\omega_{BT}}^2 \right) \left(\frac{{\omega_{BL}}^2 - {\omega_{BT}}^2}{{\omega_{AT}}^2 - {\omega_{BT}}^2} \right) \tag{4}$$

With up to three transmitted waves in the crystal, Maxwell's boundary conditions are insufficient to solve for the reflectance as a function of frequency. We must therefore use ABCs. A number of types of ABC exist, but the simplest (and generally adequate) type is the so-called "Pekar ABC" with the total polarization due to each exciton branch vanishing either at the crystal interface or at a finite distance from the crystal interface giving rise to an exciton dead-layer (with dielectric constant = ε_∞), as outlined previously [11, 12]. Thus the models presented below either ignore this dead-layer, in which case Pekar's ABC is applied at the crystal interface, or include the thickness of the dead-layer as a fitting parameter, in which case the ABC is applied at the dead-layer boundary.

Starting values in the fitting procedure for the transverse and longitudinal frequencies of the *A* and *B* excitons can be set by examination of the energy of the maximum (transverse) and minimum (longitudinal) reflectivity for the corresponding resonance feature observed experimentally. Hence, using eqns. (3) and (4), values for the static polarizability can be calculated. The static background dielectric constant and exciton mass may be obtained from the literature and are not expected to differ greatly from bulk values [18], and the static background dielectric constant may be independently estimated from the average reflection coefficient far from the exciton resonances. Solving eqn. (1) allows one to calculate the complex refractive index as a function of frequency for each propagating/evanescent wave. These refractive indices are subsequently used in the boundary condition equations below, which are solved for reflectance as a function of frequency. By varying the parameters such as longitudinal and transverse exciton energies, exciton mass, damping, etc. one may optimise the fitted reflectance spectra to the experimental data using a least squares procedure. The matrix computations detailed below may be implemented in a variety of programming environments, and we have used MATLAB [19].

3.1. Model 1 (thin-film sample)

For this simple model we considered incident and reflected rays (electric field intensities of E_I and E_R respectively) in air with refractive index n_0, and the three propagating exciton-polariton waves in ZnO predicted by eqn. (1) (E_{1-3}), where the refractive index is n_{1-3} for each mode. We assume the ZnO layer to

be semi-infinite and neglected transmitted waves into the sapphire substrate, reflected waves from the ZnO/sapphire interface and excitonic dead-layers. The modes are shown in figure 2(a).

Applying Maxwell's (eqns. (5) and (6)) and Pekar's (eqns. (7) and (8)) boundary conditions, one obtains the simultaneous equation set [11, 17]:

$$E_I + E_R = E_1 + E_2 + E_3 \tag{5}$$

$$n_0 E_I - n_0 E_R = n_1 E_1 + n_2 E_2 + n_3 E_3 \tag{6}$$

$$\alpha_A(k_1,\omega)E_1 + \alpha_A(k_2,\omega)E_2 + \alpha_A(k_3,\omega)E_3 = 0 \tag{7}$$

$$\alpha_B(k_1,\omega)E_1 + \alpha_B(k_2,\omega)E_2 + \alpha_B(k_3,\omega)E_3 = 0 \tag{8}$$

where $\alpha(k,\omega)$ is the polarizability of either the *A* or *B* free-excitons as a function of frequency for each of the three-solutions for wavevector $k_{1,2,3}$. These frequency-dependent polarizabilities are:

$$\alpha_A(k_{1-3},\omega) = \varepsilon_0(\varepsilon_\infty - 1) + \frac{\alpha_{A0}{\omega_{AT}}^2}{{\omega_{AT}}^2 + \beta_A k_{1-3}^2 - \omega^2 - i\omega\Gamma_A} \tag{9}$$

for *A* excitons, and a similar expression for *B* excitons based on eqn. (1). We re-express the boundary conditions above as the matrix equation:

$$\begin{pmatrix} r \\ A \\ B \\ C \end{pmatrix} = \begin{pmatrix} -1 & 1 & 1 & 1 \\ 1 & n_1 & n_2 & n_3 \\ 0 & \alpha_{A1} & \alpha_{A2} & \alpha_{A3} \\ 0 & \alpha_{B1} & \alpha_{B2} & \alpha_{B3} \end{pmatrix}^{-1} \begin{pmatrix} 1 \\ 1 \\ 0 \\ 0 \end{pmatrix} \tag{10}$$

where the relative field intensities are defined as; $r = E_R/E_I$, $A = E_1/E_I$, $B = E_2/E_I$ and $C = E_3/E_I$; α_{A1-3} are the frequency-dependent polarizabilities discussed above of the *A* free-excitons with wave-vectors k_{1-3}, α_{B1-3} are the frequency-dependent polarizabilities of the *B* free-excitons with wave-vectors k_{1-3}, and the refractive index of air has been set to unity. Solving this expression for the amplitude reflection coefficient *r*, one then squares the solution to obtain the reflectance. The quantities A, B and C yield the relative interface field amplitudes and phases for the 3 propagating polariton modes in the structure

3.2. Model 2 (thin-film sample)

For the second model of the PLD material we included the thin-film nature of the sample, where the film thickness is denoted by L and was used as a fitting parameter. We have also included reflected waves from the ZnO/sapphire interface, and a transmitted wave into the sapphire substrate as shown in figure 2(b). The matrix equation, derived similarly to the above case, is:

$$\begin{pmatrix} r \\ A \\ B \\ C \\ D \\ E \\ F \\ G \end{pmatrix} = \begin{pmatrix} -1 & 1 & 1 & 1 & 1 & 1 & 1 & 0 \\ 1 & n_1 & n_2 & n_3 & -n_1 & -n_2 & -n_3 & 0 \\ 0 & \mathrm{e}_1 & \mathrm{e}_2 & \mathrm{e}_3 & \mathrm{e}_1^* & \mathrm{e}_2^* & \mathrm{e}_3^* & -1 \\ 0 & n_1\mathrm{e}_1 & n_2\mathrm{e}_2 & n_3\mathrm{e}_3 & -n_1\mathrm{e}_1^* & -n_2\mathrm{e}_2^* & -n_3\mathrm{e}_3^* & -n_s \\ 0 & \alpha_{A1} & \alpha_{A2} & \alpha_{A3} & \alpha_{A1} & \alpha_{A2} & \alpha_{A3} & 0 \\ 0 & \alpha_{B1} & \alpha_{B2} & \alpha_{B3} & \alpha_{B1} & \alpha_{B2} & \alpha_{B3} & 0 \\ 0 & \alpha_{A1}\mathrm{e}_1 & \alpha_{A2}\mathrm{e}_2 & \alpha_{A3}\mathrm{e}_3 & \alpha_{A1}\mathrm{e}_1^* & \alpha_{A2}\mathrm{e}_2^* & \alpha_{A3}\mathrm{e}_3^* & 0 \\ 0 & \alpha_{B1}e_1 & \alpha_{B2}\mathrm{e}_2 & \alpha_{B3}\mathrm{e}_3 & \alpha_{B1}\mathrm{e}_1^* & \alpha_{B2}\mathrm{e}_2^* & \alpha_{B3}\mathrm{e}_3^* & 0 \end{pmatrix}^{-1} \begin{pmatrix} 1 \\ 1 \\ 0 \\ 0 \\ 0 \\ 0 \\ 0 \\ 0 \end{pmatrix} \tag{11}$$

where $e_i = \exp(i\frac{n_i\omega L}{c})$ and hence takes account of the propagation phase difference at each interface of the thin-film, with n_i representing the refractive indices n_1, n_2 or n_3. Similarly e_i^* refers to the factor $e_i^* = \exp(-i\frac{n_i\omega L}{c})$. Again the model yields the amplitude reflection coefficient and the relative amplitudes and phases of the other propagating modes at the film boundaries.

3.3. Model 3 (thin-film sample)

For the third model of the thin-film sample, we included exciton dead-layers at the air/ZnO and ZnO/sapphire interfaces with widths L_1 and L_3 respectively, where L_2 is the thickness of the ZnO thin-film itself as shown in figure 2(c). These three lengths were used as fitting parameters. The boundary conditions become substantially more complicated in this case, and are:

$$\begin{pmatrix} r \\ A \\ B \\ C \\ D \\ E \\ F \\ G \\ H \\ I \\ J \\ K \end{pmatrix} = \begin{pmatrix} -1 & 1 & 1 & 0 & 0 & 0 & 0 & 0 & 0 & 0 & 0 & 0 \\ 1 & n_D & -n_D & 0 & 0 & 0 & 0 & 0 & 0 & 0 & 0 & 0 \\ 0 & -\mathrm{e}_{D1} & -\mathrm{e}^*_{D1} & 1 & 1 & 1 & 1 & 1 & 1 & 0 & 0 & 0 \\ 0 & -n_D\,\mathrm{e}_{D1} & n_D\,\mathrm{e}^*_{D1} & n_1 & n_2 & n_3 & -n_1 & -n_2 & -n_3 & 0 & 0 & 0 \\ 0 & 0 & 0 & \mathrm{e}_{12} & \mathrm{e}_{22} & \mathrm{e}_{32} & \mathrm{e}^*_{12} & \mathrm{e}^*_{22} & \mathrm{e}^*_{32} & -1 & -1 & 0 \\ 0 & 0 & 0 & n_1\,\mathrm{e}_{12} & n_2\,\mathrm{e}_{22} & n_3\,\mathrm{e}_{32} & -n_1\,\mathrm{e}^*_{12} & -n_2\,\mathrm{e}^*_{22} & -n_3\,\mathrm{e}^*_{32} & -n_D & n_D & 0 \\ 0 & 0 & 0 & 0 & 0 & 0 & 0 & 0 & 0 & \mathrm{e}_{D3} & \mathrm{e}^*_{D3} & -1 \\ 0 & 0 & 0 & 0 & 0 & 0 & 0 & 0 & 0 & n_D\,\mathrm{e}_{D3} & -n_D\,\mathrm{e}^*_{D3} & -n_S \\ 0 & 0 & 0 & \alpha_{A1} & \alpha_{A2} & \alpha_{A3} & \alpha_{A1} & \alpha_{A2} & \alpha_{A3} & 0 & 0 & 0 \\ 0 & 0 & 0 & \alpha_{B1} & \alpha_{B2} & \alpha_{B3} & \alpha_{B1} & \alpha_{B2} & \alpha_{B3} & 0 & 0 & 0 \\ 0 & 0 & 0 & \alpha_{A1}\,\mathrm{e}_{12} & \alpha_{A2}\,\mathrm{e}_{22} & \alpha_{A3}\,\mathrm{e}_{32} & \alpha_{A1}\,\mathrm{e}^*_{12} & \alpha_{A2}\,\mathrm{e}^*_{22} & \alpha_{A3}\,\mathrm{e}^*_{32} & 0 & 0 & 0 \\ 0 & 0 & 0 & \alpha_{B1}\,\mathrm{e}_{12} & \alpha_{B2}\,\mathrm{e}_{22} & \alpha_{B3}\,\mathrm{e}_{32} & \alpha_{B1}\,\mathrm{e}^*_{12} & \alpha_{B2}\,\mathrm{e}^*_{22} & \alpha_{B3}\,\mathrm{e}^*_{32} & 0 & 0 & 0 \end{pmatrix}^{-1} \begin{pmatrix} 1 \\ 1 \\ 0 \\ 0 \\ 0 \\ 0 \\ 0 \\ 0 \\ 0 \\ 0 \\ 0 \\ 0 \end{pmatrix}$$

(12)

where the notation e_{ij} refers to the factor $\exp(i\frac{n_i\omega L_j}{c})$ with n_i representing the refractive indices $n_D(=\sqrt{\varepsilon_\infty})$, n_1, n_2 or n_3, and L_j representing the lengths L_1, L_2 or L_3. n_S denotes the refractive index of sapphire (~ 1.8 at 370 nm [20]). Similarly, the factor e^*_{ij} refers to the factor $\exp(-i\frac{n_i\omega L_j}{c})$.

3.4. Model 4 (bulk ZnO wafer)

The final model, for the bulk ZnO wafer, is similar to that of Model 1 above except that we have included an exciton dead-layer (figure 2(d)) with thickness *L*. In this case the boundary conditions are:

$$\begin{pmatrix} r \\ A \\ B \\ C \\ D \\ E \end{pmatrix} = \begin{pmatrix} -1 & 1 & 1 & 0 & 0 & 0 \\ 1 & n_D & -n_D & 0 & 0 & 0 \\ 0 & e & e^* & -1 & -1 & -1 \\ 0 & n_D e & -n_D e^* & -n_1 & -n_2 & -n_3 \\ 0 & 0 & 0 & \alpha_{A1} & \alpha_{A2} & \alpha_{A3} \\ 0 & 0 & 0 & \alpha_{B1} & \alpha_{B2} & \alpha_{B3} \end{pmatrix}^{-1} \begin{pmatrix} 1 \\ 1 \\ 0 \\ 0 \\ 0 \\ 0 \end{pmatrix} \qquad (13)$$

where $e_i = \exp(i\frac{n_i\omega L}{c})$ and $e^*_i = \exp(-i\frac{n_i\omega L}{c})$ as above.

4. Results and Discussion

Figure 3 shows the experimental reflectance data (at near-normal incidence) from each of three PLD samples at 17 K. We have labelled the spectral regions (I, II, III) in correspondence with those shown in figure 1. Although the *A* and *B* excitonic resonances are apparent in the unannealed material, one observes a relative improvement in the oscillator strengths with annealing temperatures/durations. Previous Raman and AFM measurements on these samples indicate that the unannealed sample has the smallest grain size and the largest surface roughness (standard deviation of ~ 10 nm) and that the grain size increases and the roughness decreases (to a value of ~ 3 nm) in the annealed samples [13, 14]. The decrease in the intensity of excitonic features with decreasing grain size is a consequence of the increasing effects of electric fields due to charge trapping at grain boundaries in smaller grain samples, causing substantial exciton damping [13,14]. We also observe oscillatory structures at lower ("region I") and higher ("region III") energies. On the basis of the results obtained by applying our models, discussed below, these additional oscillatory structures are due to Fabry-Perot (FP) oscillations in the thin-film [8]. We believe that the variation in visibility of the FP fringes among the PLD samples is the result of scattering at the surface (which is related to the roughness and hence the annealing conditions), which reduces the coherence between the waves from the front and back surfaces of the sample.

Figure 4 shows the experimental reflectance data of the best quality PLD sample in figure 3 above, along with the best-fits obtained using each of the models discussed above. In the case of Model 1, where we considered only a semi-infinite slab of ZnO, one finds that the excitonic resonances in region II are well-described but that the oscillatory structures in regions I and III are not. Figure 4 also shows the results of applying Model 2 to this sample, where reflected waves in the thin-film were also taken into account. This model provides a much better fit in regions I and III than Model 1, hence we have attributed the oscillations in these spectral regions to FP fringes. The film thickness was included as a fitting parameter and is determined to be ~ 215 nm, in excellent agreement with the actual thickness of ~ 200 nm [13,14]. The use of Model 3, where exciton dead-layers were included at both film boundaries, produces an identical spectrum to that of the simpler Model 2 and does not improve upon the fit.

The origin of the observed reflectance behaviour, where FP oscillations are seen at energies below and above the exciton-photon interaction region, while the central excitonic region is well described by a model neglecting the thin film nature of the sample, may be understood as follows. Figure 1 shows the dispersion of the exciton-polaritons in ZnO. FP oscillations will be observed only if the spatial damping of the propagating modes is sufficiently small that the modes can make two passes through the film. This condition is quantified by requiring that the sample thickness d is significantly less than L, where $L = \left(n_i.k_0\right)^{-1}$, n_i is the imaginary part of the mode refractive index and k_0 the free space wavevector [21]. The L values of the photon-like branches in regions I and III, where mixing with the highly damped exciton is minimal, are ~ 120,000 nm and ~ 40,000 nm respectively and $L >> 200$ nm. Thus we expect to see oscillatory structure in the reflectance. In region II, L for all modes is < 400 nm due to the large damping of the exciton and the strong exciton-photon mixing. Thus no oscillations would be expected in region II, in agreement with observation.

It should be noted that one obtains identical values for the common fitting parameters (i.e. excluding thin-film and dead-layer thicknesses), regardless of the model used. These parameters are given in table 1. Thus, increasing the complexity of boundary conditions merely enables the model to more accurately account for FP oscillations in the film rather than any refinement of the parameters governing the behaviour of the excitonic resonances.

The data computed using Model 2, shown in figure 4 provides a good qualitative fit to the experimental data, reproducing the main features of the experimental spectrum, including excitonic energy positions, FP fringe positions and the appropriate scale of the reflectance changes. However, quantitatively it may still be improved, particularly in regions I and III shown in figure 4. In particular, the models used in this paper assume single values for both exciton transverse energies and for the film thickness over its entire area and a perfectly collimated light source. Inhomogeneous strain in the sample will lead to a distribution of exciton energies in differently-strained nano-crystallites [22], and slight variations of the film thickness over the surface or departure of the light source from perfect collimation will change the form of the FP oscillations. Given the rather narrow width of the central exciton resonance (region II) of the experimental data in figure 4 and its similarity to the computed data for Models 1 and 2/3 in this region, we believe that inhomogenous

broadening of the exciton energies is less important in our samples than variations in the layer thickness over the surface and departure of the light source from perfect collimation, as both these effects lead to changes in the FP oscillatory behaviour in regions I and III, but do not affect region II to a great extent. A more detailed fitting procedure is needed to take account of these effects.

Figure 5 shows the experimental reflectance data for the bulk ZnO wafer along with the best-fit to this spectrum using Model 4, where a semi-infinite slab of material was considered and an exciton dead-layer was included. As with the PLD models above, we find that the exciton resonances are adequately described by our choice of boundary conditions. The fitting parameters are also given in table 1, and are in excellent agreement with literature values. The dead-layer parameter is important in achieving a good fit for the bulk material, while it makes no difference to the fit for the PLD samples. Hence, we believe that the high damping in the PLD material compared to bulk makes the dead-layer parameter redundant (similar to the exciton mass, discussed below), though this will not be the case for thin film material of better structural quality, e.g. grown on closely lattice-matched substrates such as ScAlMgO4 (SCAM) [23]. For higher quality thin-film samples the use of Model 3, including dead-layers at the film interfaces, will be important in achieving good agreement between theory and experiment.

A comparison of parameters for the PLD and bulk material reveals that there are significant shifts in the exciton transverse energies in the PLD material and also a substantial difference in the transverse *A*-*B* splitting, due to both biaxial strain arising from lattice mismatch with the substrate and grain boundary electric fields in the thin-film material [13,14]. The LT splitting of the *B*-exciton in the PLD sample is also very different to the value in the bulk crystal. The physical origin of such a dramatic difference is not clear. While the combination of strain and electric fields in these samples is a possible explanation, it is more likely to be due to the effects of inhomogeneous broadening of the exciton resonance and varying layer thickness/source collimation effects discussed above. In particular, it is clearly seen that the exciton damping factors for the *A*- and *B*-excitons in the PLD sample are much larger than the values in the bulk sample as expected on the basis of the significantly poorer crystal quality of the PLD material and the small grain sizes. These damping parameters serve as an excellent measure of the optical quality of the material, and, due to the associated spatial damping discussed previously, will indicate the potential of such samples for

applications in random lasing or polariton lasing structures [4, 5]. Based on the figure for spatial damping (< 400nm) given earlier, the PLD films studied in this work would not be suitable for cavity polariton effects to be seen, as the film thickness is of the same order of magnitude as the damping length. Thin films of significantly better quality, e.g. grown on substrates with better lattice matching, are expected to demonstrate such effects [23, 24]. However, the damping length is significantly larger than the grain size (~ 80 nm) and thus the film may be expected to show random lasing behaviour due to multiple scattering at grain boundaries, under high level excitation. In fact, random lasing has been reported by our group in this film, in agreement with this prediction [25]. The exciton effective mass calculated for the PLD sample is 0.5 times the electron mass (m_e), significantly different to the value found for the bulk material of 0.9 m_e (as found in the literature also). However, it is known that in samples with high damping the effects of spatial dispersion on the reflectance spectra are strongly reduced [8] and the fit is largely insensitive to this parameter. A visually identical spectrum is computed using the bulk value of the exciton effective mass.

5. Conclusions

We have used a two-band dielectric response function to model normal incidence reflectance spectra from bulk and thin-film ZnO samples. We have presented in detail a number of models of the thin-film material and have given boundary conditions that include or omit Fabry-Perot oscillations in the film and/or excitonic dead-layer effects. We obtain good qualitative fits to the excitonic resonance features and, when reflections in the thin-film are included, good fits in higher and lower energy regions. The fitting parameters of these models can be compared for different thin-film samples, and compared to those of bulk wafers. Thus, the analysis of reflectance spectra using these models provides an optical means of simultaneously determining film-thickness and a quantitative means of comparing sample ‘quality’. We find that it is important to consider the full polariton picture in interpreting the reflectance spectra of nanocrystalline ZnO material. Although we have used the models to solve solely for the reflectance, they can also be used to determine electric fields due to different photon and polariton modes in the structure also.

The application of such fitting procedures to reflectance data from nanocrystalline thin films enables a quantitative estimation of the suitability of such nanostructured materials for applications such as random lasing and polariton lasing structures.

Acknowledgements

The authors acknowledge financial support from the Higher Education Authority under the NDP, and from the School of Physical Sciences, DCU and also acknowledge the generous supply of PLD-grown samples from Prof. J G Lunney and Dr. E dePosada of Trinity College Dublin, Ireland.

References

[1] D.C. Reynolds, D.C. Look, B. Jogai, R.L. Jones, C.W. Litton, W. Harsch and G. Cantwell, J. Lumin. **82**, 173 (1999).

[2] N.N. Syrbu, I.M. Tiginyanu, V.V. Ursaki, V.V. Zalamai, Veaceslav Popa , S.M. Hubbard and Dimitris Pavlidis, MRS Internet J. Nitride Semicond. Res. **8**, 1 (2003).

[3] P.P. Paskov, T. Paskova, P.O. Holtz and B. Monemar, Phys. Stat. Sol. (a) **201**, 678 (2004).

[4] M. Zamfirescu, A. Kavokin, B. Gil, G. Malpuech, and M. Kaliteevski, Phys. Rev. B **65**, 161205 (2002).

[5] H. Cao, Y. G. Zhao, S. T. Ho, E. W. Seelig, Q. H. Wang, and R. P. H. Chang, Phys. Rev. Lett. **82**, 2278 (1999).

[6] J.J. Hopfield and D.G. Thomas, Phys. Rev. Lett. **15**, 22 (1965).

[7] R. Kuhnert, R. Helbig and K. Hummer, Phys. Stat. Sol. (b) **107**, 83 (1981).

[8] V.A. Kiselev, B.S. Razbirin and I.N. Uralstev, Phys. Stat. Sol. (b) **72**, 161 (1975).

[9] S.J. Pearton, D.P. Norton, K. Ip, Y.W. Heo and W. Steiner, Prog. Mater. Sci. **50** 293 (2005).

[10] E. McGlynn, J. Fryar, M. O. Henry, J.-P.Mosnier, J. G. Lunney, D. O' Mahony and E.dePosada, Physica B **340-342C** 230 (2003).

[11] J. J. Hopfield and D. G. Thomas. Phys. Rev. **132**, 563-572 (1963).

[12] S.I. Pekar, Sov. Phys.-Solid State **4**, 953 (1962).

[13] E. McGlynn, J. Fryar, G. Tobin, C. Roy, M.O. Henry, J-P. Mosnier, E. dePosada and J.G. Lunney , Thin Solid Films **458,** 330 (2004).

[14] C. Roy, S. Byrne, E. McGlynn, J-P Mosnier, E. de Posada, D. O'Mahony, J. G. Lunney, M. Henry, B. Ryan and A.A. Cafolla, Thin Solid Films **436** 273 (2003).

[15] W. R. L. Lambrecht, A. V. Rodina, S. Limpijumnong, B. Segall and B. K. Meyer, Phys. Rev. B **65**, 075207 (2002).

[16] D.G. Thomas, J. Phys. Chem. Solids **15**, 86 (1960); J.J. Hopfield, J. Phys. Chem. Solids **15**, 97 (1960).

[17] J. Lagois, Phys. Rev. B **16**, 1699-1705 (1977).

[18] B.K. Meyer, H. Alves, D.M. Hofmann, W. Kriegseis, D. Forster, F. Bertram, J. Christen, A. Hoffmann, M. Strassburg, M. Dworzak, U. Haboeck and A.V. Rodina, Phys. Stat. Solidi (b) **241**, 231 (2004).

[19] http://www.mathworks.com/

[20] D. Hofstetter and R. L. Thornton, IEEE J. Quant. Elec. **34**, 1914 (1998); M. E. Thomas, S. K. Andersson, R. M. Sova and R. I. Joseph, Infrared Physics & Technology **39,** 185 (1998).

[21] E.L. Ivchenko, in: Excitons, ed. E.I. Rashba and M.D. Sturge, North-Holland, Amsterdam, 1982, pp. 141-176.

[22] J. Lagois, Phys. Rev. B **23**, 5511 (1981).

[23] A. Tsukazaki, A. Ohtomo, S. Yoshida, M. Kawasaki, C. H. Chia, T. Makino, Y. Segawa, T. Koida, S. F. Chichibu and H. Koinuma, Appl. Phys. Lett. **83**, 2784 (2003); T. Makino, K. Tamura, C. H. Chia, Y. Segawa, M. Kawasaki, A. Ohtomo and H. Koinuma, Appl. Phys. Lett. **81**, 2172 (2002).

[24] S. F. Chichibu, A. Uedono, A. Tsukazaki, T. Onuma, M. Zamfirescu, A. Ohtomo, A. Kavokin, G. Cantwell, C.W. Litton, T. Sota and M. Kawasaki, Semicond. Sci. Technol. **20,** S67 (2005).

[25] G. Tobin, E. McGlynn, M. O. Henry, J. P. Mosnier, J. G. Lunney, D. O'Mahony and E. dePosada, Physica B **340-342**, 245 (2003).

Tables

Table 1: Fit parameters for bulk & PLD samples using two band exciton model. Final column gives literature values for ZnO single crystal.

Parameter	Bulk crystal	PLD sample (fit using model 2 discussed in text)	Literature value [17,18]
$\hbar\varpi_{AT}$ (transverse A exciton energy, eV)	3.375	3.378	3.3758
$\hbar\varpi_{BT}$ (transverse B exciton energy, eV)	3.381	3.390	3.3810
$\hbar\varpi_{AT}$ - $\hbar\varpi_{BT}$ (A-B splitting, meV)	6	12.	5.2
Δ_{LT}^{A} (A exciton LT splitting, meV)	2	2	1.8
Δ_{LT}^{B} (B exciton LT splitting, meV)	12	4	10.2
$\hbar\Gamma_{A}$ (A exciton damping, meV)	1	7	0.7
$\hbar\Gamma_{B}$ (B exciton damping, meV)	1	14	0.7
M (multiples of electron mass)	0.9	0.5	0.87
Dead-layer thickness (nm)	4	0	4

Figure Captions

Figure 1: Dispersion of the exciton-polaritons associated with the *A*- & *B*-excitons in ZnO. The upper, lower and mixed branches are shown, as are the energy regions, marked "I", "II" & "III".

Figure 2: Photon and polariton modes for; (a) Model 1; (b) Model 2; (c) Model 3; (d) Model 4. The electric field amplitudes are labelled E_j. The relative field amplitudes are labelled (1, r, A, B,…) in parentheses, corresponding to the labelling in equations (10) to (13) for Models 1 to 4, respectively in the text. Refractive index values (n) and layer thicknesses (L) are also indicated in the figure.

Figure 3: Experimental reflectance data for PLD samples at 17 K. The data are offset for clarity by 0.5 and 0.25 for the unannealed sample and the sample annealed at 400^0C for 10 minutes, respectively. The vertical scale is correct for the sample annealed at 500^0C for 15 minutes.

Figure 4: Comparison of the reflectance spectra of the PLD sample annealed at 500^0C for 15 minutes with computed reflectance spectra; without including thin-film interference effects (Model 1); including thin film interference effects (Models 2 & 3). The data are offset for clarity by 0.6 and 0.3 for the Model 1 fit and the sample annealed at 500^0C for 15 minutes, respectively. The vertical scale is correct for the Models 2 & 3 fits. Model parameters are given in table 1.

Figure 5: Comparison of the reflectance spectra of the single crystal bulk ZnO sample with the best fit calculated using Model 4. The best fit data are offset by 0.3 for clarity and the vertical scale is correct for the single crystal bulk ZnO sample. Model parameters are given in table 1. At higher photon energies the fit is poor due to the contribution of excitonic excited and other higher lying states which are not included in the fitting model.

Figure 1 – Fryar et al.

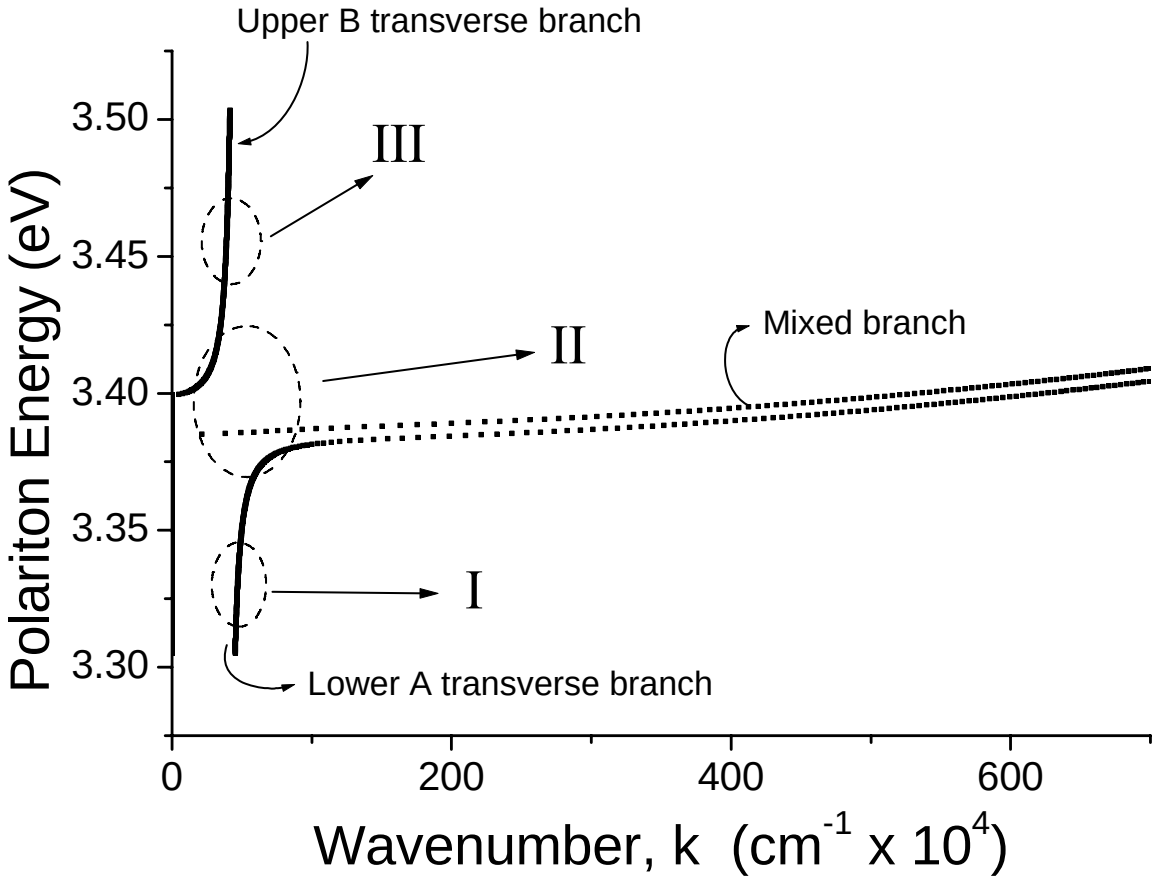

Figure 2 – Fryar et al.

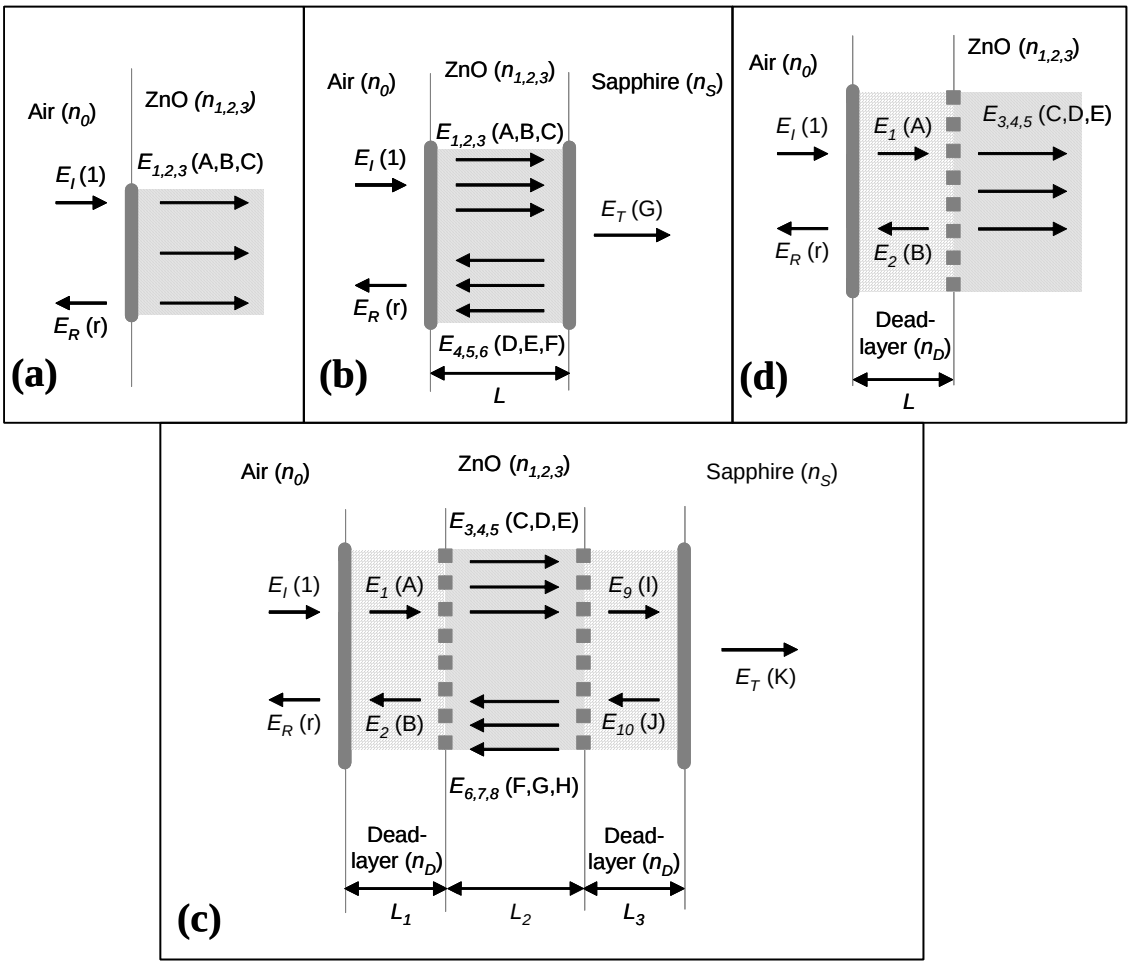

Figure 3 – Fryar et al.

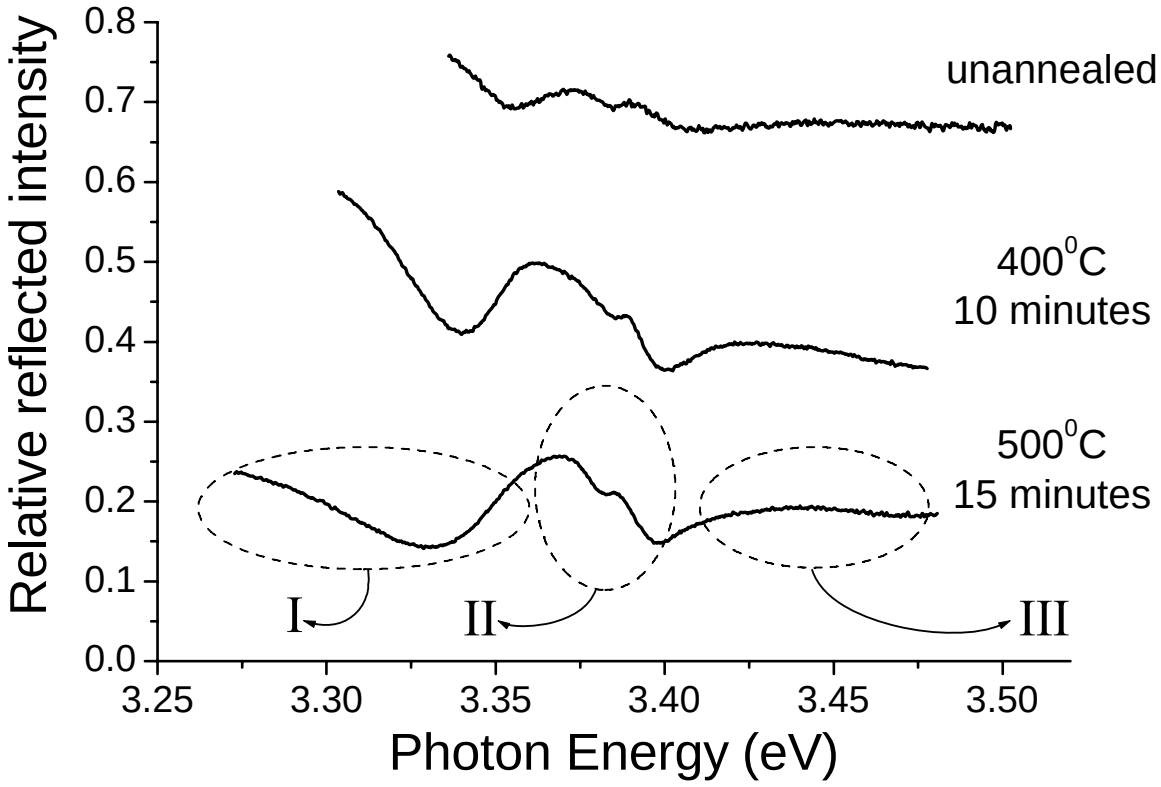

Figure 4 – Fryar et al.

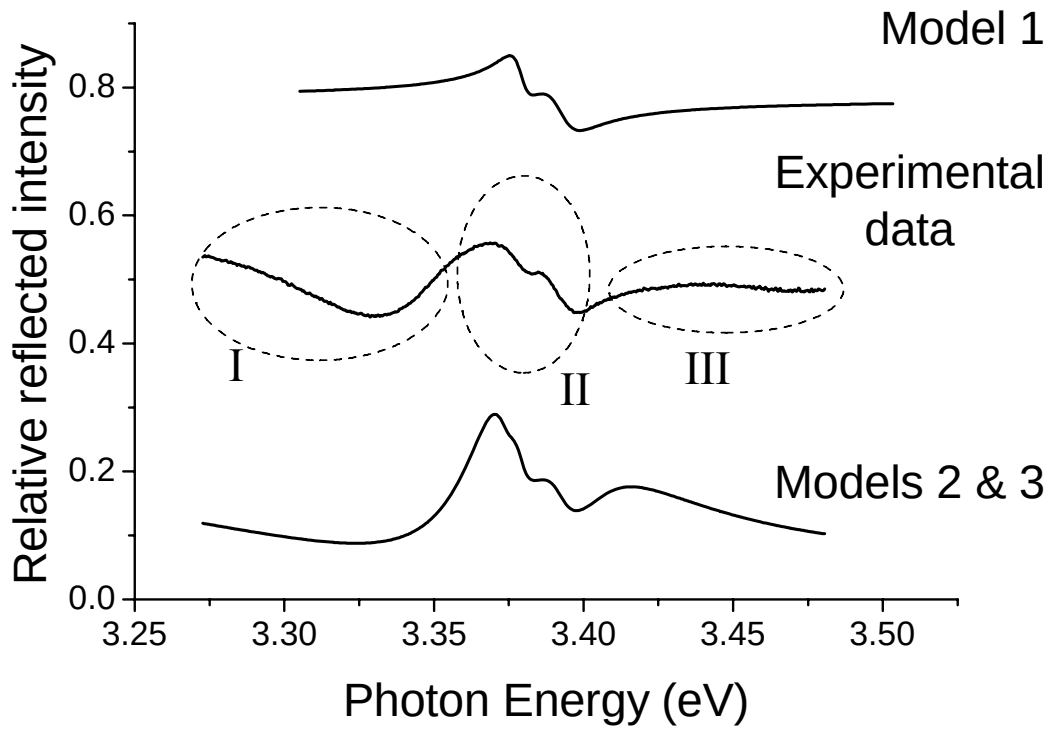

Figure 5 – Fryar et al.